

Vortex beam generation by spin-orbit interaction with Bloch surface waves

Original

Vortex beam generation by spin-orbit interaction with Bloch surface waves / Stella, U., Grosjean, T., De Leo, N., Boarino, L., Munzert, P., Lakowicz, J.R., Descrovi, E.. - In: ACS PHOTONICS. - ISSN 2330-4022. - (2020).
[10.1021/acsp Photonics.9b01625]

Availability:

This version is available at: 11583/2796661 since: 2020-02-23T11:07:40Z

Publisher:

American Chemical Society

Published

DOI:10.1021/acsp Photonics.9b01625

Terms of use:

This article is made available under terms and conditions as specified in the corresponding bibliographic description in the repository

Publisher copyright

(Article begins on next page)

Article

Vortex beam generation by spin-orbit interaction with Bloch surface wavesUgo Stella, Thierry Grosjean, Natascia De Leo, Luca Boarino,
Peter Munzert, Joseph R. Lakowicz, and Emiliano DescroviACS Photonics, **Just Accepted Manuscript** • DOI: 10.1021/acsp Photonics.9b01625 • Publication Date (Web): 10 Feb 2020Downloaded from pubs.acs.org on February 10, 2020**Just Accepted**

“Just Accepted” manuscripts have been peer-reviewed and accepted for publication. They are posted online prior to technical editing, formatting for publication and author proofing. The American Chemical Society provides “Just Accepted” as a service to the research community to expedite the dissemination of scientific material as soon as possible after acceptance. “Just Accepted” manuscripts appear in full in PDF format accompanied by an HTML abstract. “Just Accepted” manuscripts have been fully peer reviewed, but should not be considered the official version of record. They are citable by the Digital Object Identifier (DOI®). “Just Accepted” is an optional service offered to authors. Therefore, the “Just Accepted” Web site may not include all articles that will be published in the journal. After a manuscript is technically edited and formatted, it will be removed from the “Just Accepted” Web site and published as an ASAP article. Note that technical editing may introduce minor changes to the manuscript text and/or graphics which could affect content, and all legal disclaimers and ethical guidelines that apply to the journal pertain. ACS cannot be held responsible for errors or consequences arising from the use of information contained in these “Just Accepted” manuscripts.

Vortex beam generation by spin-orbit interaction with Bloch surface waves

Ugo Stella¹, Thierry Grosjean², Natascia De Leo³, Luca Boarino³, Peter Munzert⁴, Joseph R. Lakowicz⁵ and Emiliano Descrovi^{1*}

¹ Department of Applied Science and Technology (DISAT), Politecnico di Torino, Corso Duca degli Abruzzi 24, Torino, IT-10129, Italy.

² FEMTO-ST Institute, Université Bourgogne Franche-Comté, UMR CNRS 6174 15B Avenue des Montboucons, 25030, Besançon, France

³ Quantum Research Labs & Nanofacility Piemonte, Advanced Materials Metrology and Life Science Division, Istituto Nazionale di Ricerca Metrologica (INRiM), Strada delle Cacce 91, Torino, IT-10135, Italy.

⁴ Fraunhofer Institute for Applied Optics and Precision Engineering IOF, Albert-Einstein-Str. 7, Jena DE-07745, Germany

⁵ Center for Fluorescence Spectroscopy, Department of Biochemistry and Molecular Biology, University of Maryland School of Medicine, Baltimore, Maryland 21201, United States

Mr. Ugo Stella: ugo.stella@polito.it

Dr. Thierry Grosjean: thierry.grosjean@univ-fcomte.fr

Dr. Natascia De Leo: n.deleo@inrim.it

Dr. Luca Boarino: l.boarino@inrim.it

Dr. Peter Munzert: peter.munzert@iof.fraunhofer.de

Prof. Joseph R. Lakowicz: JLakowicz@som.umaryland.edu

Corresponding Author:

Prof. Emiliano Descrovi: emiliano.descrovi@polito.it

Phone: +39 011 090 7352

Fax: +39 011 090 7399

Keywords: Chiral nanostructures, Bloch Surface Waves, vortex beam, spiral diffraction gratings, azimuthally polarized beam.

ABSTRACT

Axis-symmetric grooves milled in metallic slabs have been demonstrated to promote the transfer of Orbital Angular Momentum (OAM) from far- to near-field and vice versa, thanks to spin-orbit coupling effects involving Surface Plasmons (SP). However, the high absorption losses and the polarization constraints, which are intrinsic in plasmonic structures, limit their effectiveness for applications in the visible spectrum, particularly if emitters located in close proximity to the metallic surface are concerned. Here, an alternative mechanism for vortex beam generation is presented, wherein a free-space radiation possessing OAM is obtained by diffraction of Bloch Surface Waves (BSWs) on a dielectric multilayer. A circularly-polarized laser beam is tightly focused on the multilayer surface by means of an immersion optics, such that TE-polarized BSWs are launched radially from the focused spot. While propagating on the multilayer surface, BSWs exhibit a spiral-like wavefront due to the Spin-Orbit Interaction (SOI). A spiral grating surrounding the illumination area provides for the BSW diffraction out-of-plane and imparts an additional azimuthal geometric phase distribution defined by the topological charge of the spiral structure. At infinity, the constructive interference results into free-space beams with defined combinations of polarization and OAM satisfying the conservation of the Total Angular Momentum, based on the incident polarization handedness and the spiral grating topological charge. As an extension of this concept, chiral diffractive structures for BSWs can be used in combination with surface cavities hosting light sources therein.

1
2
3 52 Vortex beams represent a family of structured beams generally characterized by a phase singularity
4
5 53 along the optical axis, a doughnut intensity distribution and an azimuthally-varying phase over a beam
6
7
8 54 transverse cross-section.^{1,2} When the polarization state is spatially inhomogeneous, the term Vectorial
9
10 55 Vortex Beams is often used.³ From a quantum-optics perspective, each vortex beam photon is
11
12 56 provided with a quantized Orbital Angular Momentum (OAM) equal to $\hbar\ell$, where ℓ is either a
13
14
15 57 positive or negative integer indicating the topological charge of the vortex. In recent years, vortex
16
17 58 beams have gained an increasing popularity because of several new applications into different
18
19 59 domains such as micro-particle manipulation and trapping,⁴⁻⁶ compact laser sources,^{7,8} microscopy^{9,10}
20
21 60 and optical communications.^{11,12} Conventional methods for producing vortex beams¹³ involve the
22
23 61 use of (possibly tunable) anisotropic media such as Liquid Crystal^{14,15} and q-plates¹⁶ or hierarchically
24
25 62 structured holograms encoding proper phase functions.¹⁷⁻²⁰ More recently, metasurfaces, which can
26
27 63 be either dielectric or plasmonic, have been introduced in order to gather more degrees of freedom in
28
29 64 OAM manipulation,^{21,22} through the control of the so-called Spin-Orbit Interaction (SOI)²³ mediated
30
31 65 by the metasurface topology.²⁴ Metasurfaces are mainly employed as free-space beam converters,
32
33 66 which have found applications also within laser cavities.²⁵ The concept of beam conversion through
34
35 67 metasurfaces relies on a spatially-dependent phase manipulation of the scattered field. The output
36
37 68 vortex beams result from a coherent sum of the scattered radiation originating from different portions
38
39 69 of the surface, which is illuminated as a whole. Despite the very high-efficiency capabilities for
40
41 70 generating vortex beams both in transmission^{26,27} and reflection,²⁸ metasurface-based approaches can
42
43 71 be hardly adopted when the input field has a limited spatial extension (as for localized sources), unless
44
45 72 some collective mode coupling is intervening.²⁹ This is indeed the case in structured metallic films,
46
47 73 wherein the generation of free-space vortex beam carrying OAM occurs upon SOI and
48
49 74 scattering/diffraction of plasmonic modes by means of nano-slits,^{30,31} properly arranged nano-
50
51 75 apertures,³² possibly combined with circular^{33,34} or spiral³⁵ diffraction gratings. Such results rely on
52
53 76 the fact that the Angular Momentum (AM) possessed by surface plasmons can be further manipulated
54
55 77 and transferred to freely propagating radiation.^{31,35}

1
2
3 78 Here we propose an alternative way of producing vortex beam, by exploiting Bloch Surface Waves
4
5 79 (BSW)^{36,37} on dielectric multilayers as a mean to transfer energy, momentum and AM to a free-space
6
7 80 propagating beam. Such a two-step process involves a Spin Angular Momentum (SAM)-to-OAM
8
9 81 conversion from a focused circularly polarized beam into radially propagating BSWs and a BSW
10
11 82 diffraction in free-space, with the additional phase distribution imparted by a chiral diffraction grating.
12
13 83 Such a BSW-based approach can benefit from the multilayer low absorption that is potentially
14
15 84 suitable for light source integration and an additional degree of freedom in the polarization state of
16
17 85 coupled BSWs, which can be either TE- or TM-polarized depending on the multilayer design.³⁸ For
18
19 86 example, a directional coupling of BSWs promoted by a magnetic spin-orbit interaction has been
20
21 87 recently demonstrated.³⁹
22
23
24
25
26 88 The setup and the sample structure are shown in Figure 1 and described in detail in the Methods
27
28 89 section. Briefly, in Figure 1a, a circularly polarized Gaussian CW laser beam ($\lambda=532$ nm) is expanded
29
30 90 and spatially filtered by means of a properly sized circular Beam Blocker. An oil-immersion, high
31
32 91 NA objective is back-contacted to a multilayer glass substrate, in order to focus the incoming beam
33
34 92 onto a flat area of the top surface, surrounded by a periodic annular grating. The multilayer is made
35
36 93 of a stack of multiple Ta₂O₅ and SiO₂ layers, topped by a 75 nm-thick PMMA film (Figures 1b,c).
37
38 94 Thanks to the beam blocker, only focused light propagating at angles larger than the glass/air critical
39
40 95 angle θ_c can reach the sample. A fraction of the incoming power is thus available for coupling to
41
42 96 BSWs, provided that wavelength, momentum and polarization matching conditions are fulfilled, as
43
44 97 indicated by the BSW dispersion curve for TE-polarization.⁴⁰ The transverse size of the focused spot
45
46 98 is sub-micron, while the central flat area surrounded by the annular grating is 6 μm wide, such that
47
48 99 the grating plays no role in the BSW coupling. Since the coupling mechanism is polarization-
49
50 100 dependent and the incident electric field is circularly polarized, BSWs are spreading radially from the
51
52 101 focused spot area, with an accumulated phase delay that is linearly varying with the azimuthal angle
53
54 102 of the propagation direction. As a result of the SAM-to-OAM transfer, a BSW propagating radially
55
56
57
58
59
60

1
2
3 103 on the multilayer surface is obtained, with a peculiar spiral-like wavefront profile (see Supporting
4
5 104 Information), analogous to plasmonic vortices.⁴¹ Surrounding the flat coupling region, a diffractive
6
7
8 105 grating is etched in the PMMA layer. The grating operates as an outcoupler, by diffracting BSWs
9
10 106 out-of-plane in both substrate (glass) and cladding (air) media, along a direction close-to-normal to
11
12 107 the sample surface (order of diffraction $n=-1$).⁴² Depending on the grating shape (e.g. circular or
13
14
15 108 spiral-like), an additional phase profile can be imparted to the diffracted radiation. In previous
16
17 109 applications, this feature has been exploited for steering the diffracted beam.^{43,44} The outcoupled
18
19 110 power is then collected by the same high-NA objective and Fourier-transformed before being imaged
20
21 111 on the camera plane. A linear polarizer and a quarter-wave plate allow for a polarization analysis on
22
23
24 112 the collected images. If the beam blocker is removed, an interference pattern as shown in Figure 1a
25
26 113 can be obtained. In this example, the spiral-shaped interference fringes result from the superposition
27
28 114 of a diffracted vortex beam (charge $\ell = 1$) and light reflected from the sample surface.³⁵

30
31 115 [FIGURE 1]

32
33 116 **Figure 1.** a) Sketch of the experimental setup. L1-4 Plano-Convex lenses, LP_{1,2} Polarizers, QW_{1,2}
34
35 117 Quarter-wave Plates, BB Beam Blocker, BS Beamsplitter, BFP Back Focal Plane. In the exemplary
36
37 118 BFP image, an interference pattern is shown, due to the superposition of a diffracted vortex beam and
38
39 119 a reflected spherical wave from the sample surface. No Beam Blocker has been used in this case. b)
40 120 Detailed view of the BSW coupling and diffraction mechanism. Illumination is provided by means
41
42 121 of a beam-blocked circularly polarized laser beam focused through an oil immersion objective, such
43
44 122 that the minimum incidence angle is slightly above the critical angle θ_c , in order to match the BSW
45 123 coupling conditions. c) Sketch of the multilayer structure with an exemplary spiral diffraction grating
46
47 124 fabricated in PMMA on top (not to scale).

50 126 RESULTS AND DISCUSSION

51
52
53 127 In this section, experimental results are presented related to (i) a circular-symmetric annular grating
54
55 128 with topological charge $m=0$, (ii) a single-arm spiral grating, (iii) a double-arm spiral grating. In the
56
57 129 last two cases, both handedness of the incident polarization are considered, namely Right-Handed
58
59 130 Circular (RHC) and Left-Handed Circular (LHC) polarizations, such that the incident beam SAM and

the grating topological charge can have either equal or opposite sign. In order to evaluate the polarization state of the diffracted light, the polarization ellipse parameter $\varepsilon(k_x, k_y) = \frac{1}{2} \arg(\sqrt{S_1^2 + S_2^2} + iS_3)$ is calculated across the Back Focal Plane (BFP), where S_1 , S_2 and S_3 are the Stokes parameters.⁴⁵ Right-Handed Circular (RHC), Left-Handed Circular (LHC) and Linear Polarizations (LP) correspond to $\varepsilon_{RHC} = \frac{\pi}{4}$, $\varepsilon_{LHC} = -\frac{\pi}{4}$ and $\varepsilon_{LP} = 0$ respectively. Polarization-filtered raw images and Stokes parameter distributions for the structures considered here are shown in the Supporting Information.

A numerical 3D model based on a commercial Finite-Difference Time-Domain (FDTD) solver (Lumerical Inc.) is used to support the interpretation of the experimental observations. In order to mimic the focused circularly polarized beam underlying the BSW coupling, a pair of (coherent) linear orthogonal dipoles laying on the multilayer plane and oscillating with a $\frac{\pi}{2}$ relative phase delay are introduced (see Supporting Information Movie S2). Further details on the validity of this model are provided in the Methods section.

Circular Outcoupler (m=0). In this configuration, a RHC circular polarization ($\varepsilon = \frac{\pi}{4}$) is employed to couple BSWs that are then diffracted. As shown in Figures 2a,e, the total intensity collected on the BFP exhibits a maximum at $k_x=k_y=0$, corresponding to a constructive interference condition for light traveling along a direction perpendicular to the multilayer surface. A linear-polarization filtering reveals the presence of a pair of spiral-like fringes spreading from the central maximum that rotate as the polarization analyser is rotated (in Figures 2b,f the measured and calculated intensity of the x-component of the diffracted light are presented). Without the polarization filter, the spiral-like fringes merge together to form a ring surrounding the central maximum. When polarization-projected onto a RHC polarization state, the intensity pattern has still a maximum in the BFP center (Figures 2c,g), while a weak ring is obtained for a projection onto a LHC polarization state (Figures 2d,h). A comparison between the distributions for the measured and the calculated parameter $\varepsilon(k_x, k_y)$ on the

1
2
3
4 155 BFP indicates that the central maximum is substantially RHC polarized, i.e. $\varepsilon(0,0) \cong \frac{\pi}{4}$. The
5
6 156 polarization state is smoothly flipping to LHC (i.e. $\varepsilon(0,0) \cong -\frac{\pi}{4}$) while moving radially from the
7
8
9 157 center (Figures 2i,l).
10
11 158 By enforcing the conservation of the Total Angular Momentum J , which also takes into account the
12
13 159 topological charge m imparted by the diffraction grating, the following equation applies: $\sigma_i + m =$
14
15
16 160 $1 + 0 = \sigma_o + \ell$, where σ_o is the output SAM number and ℓ is the corresponding OAM number. The
17
18 161 solution to this equation is not unique. In particular, two SAM-OAM configurations are possible: a
19
20 162 RHC beam preserving the input polarization and carrying zero OAM, i.e. $\sigma_o = +1$ and $\ell = 0$, and a
21
22 163 doughnut LHC beam with a reverse polarization, with $\sigma_o = -1$ and OAM with $\ell = +2$. The two
23
24 164 beams are partially overlapped, thus explaining the polarization state change from RHC to LHC along
25
26 165 a radial direction,³⁵ as illustrated above. This observation is supported by the phase distribution
27
28 166 calculated for the RHC and the LHC polarized fields presented in Figures 2m,n: a flat wavefront with
29
30 167 constant phase is found for the RHC beam ($\ell = 0$) and a spiral wavefront with two 2π discontinuities
31
32 168 for the LHC beam ($\ell = +2$).
33
34
35
36

37 169 [FIGURE 2]
38

39 170 **Figure 2.** BFP Diffraction patterns from a circular outcoupler ($m = 0$). Incident polarization is RHC.
40
41 171 a,e) experimental and calculated total intensity showing a central spot surrounded by a weak outer
42
43 172 ring; b,f) experimental and calculated x-polarized intensity; c,g) experimental and calculated RHC
44
45 173 intensity showing a central spot; d,h) experimental and calculated LHC intensity showing a doughnut
46
47 174 shape; i,l) experimental and calculated polarization ellipse parameter $\varepsilon(k_x, k_y)$ with the sign reversal
48
49 175 from the inner area to the outer ring; m) calculated phase of the diffracted field with RHC polarization,
50
51 176 showing a constant distribution; n) calculated phase of the diffracted field with LHC polarization,
52
53 177 showing two 2π discontinuities (vortex charge $\ell = +2$).
54

55
56 179 **Spiral Outcoupler ($m = -1$).** BSWs are first coupled with an input RHC polarization ($\sigma_i = +1$)
57
58 180 and made interacting by a spiral grating with opposite handedness ($m = -1$). The corresponding
59
60 181 intensity pattern is shown in Figures 3a,e.

[FIGURE 3]

Figure 3. BFP Diffraction patterns from a 1-arm spiral outcoupler ($m = -1$). Incident polarization is RHC. a,e) experimental and calculated total intensity showing a doughnut shape; b,f) experimental and calculated x-polarized intensity; c,g) experimental and calculated y-polarized intensity; d,h) experimental and calculated 45°-polarized intensity; i,l) experimental and calculated polarization ellipse parameter $\varepsilon(k_x, k_y)$ indicating a substantially linear polarization state $\varepsilon \cong 0$; m,n) experimental and calculated ellipse parameter $\alpha(k_x, k_y)$ indicating an azimuthal orientation of the electric field.

The phase delay profile imparted by the diffractive structure onto the diffracted BSWs results in a destructive interference such that a zero-intensity phase singularity is produced at $k_x = k_y = 0$. When filtered with the linear polarizer LP_1 (e.g. oriented along the x, y or 45° direction), two-lobe patterns are found, whose orientation is perpendicular to the analyzer transmission axis (Figures 3b-d). Calculated intensity patterns are in good agreement with the experimental observations (Figures 3f-h). The distribution of the parameter $\varepsilon(k_x, k_y)$ shows a substantially linear polarization corresponding to the doughnut ($\varepsilon \cong 0$) (Figures 3i,l). The uniformity of the polarization orientation is evaluated by extracting the parameter $\alpha(k_x, k_y) = \frac{1}{2} \arg(S_1 + iS_2)$, which provides the local orientation of the polarization ellipse (almost a line, in this case) across the BFP.⁴⁵ In Figures 3m,n both the experimental and the calculated distributions for $\alpha(k_x, k_y)$ indicate that the substantially linear polarization follows an axis-symmetric distribution such that the electric field is azimuthally oriented about the beam axis in $k_x = k_y = 0$. In this case, the J conservation rule reads as $\sigma_i + m = 1 - 1 = \sigma_o + \ell = 0$, leading to two fully overlapped beams with SAM $\sigma_o = +1$ and OAM $\ell = -1$ and $\sigma_o = -1$ and OAM $\ell = +1$, respectively (see Figures S6e,f and Figures S7e,f in Supporting Information). The coherent superposition of such beams having circular, yet orthogonal, polarizations is consistent with the observed azimuthal polarization state of the output beam.

When the illumination polarization is switched to LHC ($\sigma_i = -1$) the input SAM and the grating topological charge possess the same sign. The overall intensity pattern having a doughnut shape is

1
2
3 208 presented in Figures 4a,e. At a closer look, the output results from the superposition of a pair of ring-
4
5 209 shaped beams, which are non-interfering because of their orthogonal polarizations. A weak outer ring
6
7
8 210 (Figures 4c,g) is imaged upon RHC filtering, while an intense inner ring (Figures 4d,h) is obtained
9
10 211 upon LHC filtering. The experimental and the calculated distributions for $\varepsilon(k_x, k_y)$ (Figures 4i,l)
11
12 212 confirm that the polarization state of the two beams is still substantially circular. However, a reversal
13
14
15 213 of handedness from LHC to RHC can be found while moving from the inner ring toward the outer.
16
17 214 The two partially overlapped beams must satisfy the J conservation rule, i.e. $\sigma_i + m = -1 - 1 = \sigma_o$
18
19 215 $+ \ell = -2$. A first solution to this equation is represented by a LHC polarized beam having the same
20
21
22 216 SAM number as the incident radiation $\sigma_o = -1$ and OAM $\ell = -1$ (Figures 4d,h). An orthogonal
23
24 217 solution is a RHC polarized beam having a reversed SAM $\sigma_o = +1$ and OAM $\ell = -3$ (Figures 4c,g).
25
26
27 218 The topological charge of the diffracted vortex beams can be directly appreciated from the calculated
28
29 219 phase distributions of the RHC and LHC polarized beams (Figures 4m,n), exhibiting three and one
30
31 220 2π discontinuities respectively, on the BFP.

33
34 221 [FIGURE 4]

35
36 222 **Figure 4.** BFP Diffraction patterns from a 1-arm spiral outcoupler ($m = -1$). Incident polarization is
37
38 223 LHC. a,e) experimental and calculated total intensity showing a superposition of an inner and an outer
39
40 224 ring-shaped patterns; b,f) experimental and calculated x-polarized intensity; c,g) experimental and
41
42 225 calculated RHC intensity, distributed according to the outer ring; d,h) experimental and calculated
43
44 226 LHC intensity; distributed according to the inner ring; i,l) experimental and calculated polarization
45
46 227 ellipse parameter $\varepsilon(k_x, k_y)$ indicating a substantially circular polarization with handedness reversal
47
48 228 from the inner to the outer ring; m) calculated phase of the diffracted field with RHC polarization,
49
50 229 showing three 2π discontinuities; n) calculated phase of the diffracted field with LHC polarization,
51
52 230 showing one 2π discontinuity.

53 232 **Spiral Outcoupler ($m = -2$).** As in the previous configuration, an incident RHC polarization (σ_i
54
55
56 233 $= +1$) is first considered. The overall intensity shown in Figures 5a,e is obtained as the superposition
57
58 234 of a weak outer ring and a brighter central spot. Both patterns can be individually imaged by operating
59
60

1
2
3 235 a polarization filtering through a RHC state (Figures 5c,g) and a LHC state (Figures 5d,h),
4
5 236 respectively.

7
8 237 [FIGURE 5]

10 238 **Figure 5.** BFP Diffraction patterns from a 2-arms spiral outcoupler ($m = -2$). Incident polarization
11 is RHC. a,e) experimental and calculated total intensity, given by the superposition of a central spot
12 239 and a weaker outer ring; b,f) experimental and calculated x-polarized intensity; c,g) experimental and
13 240 calculated RHC intensity, distributed according to the weak outer ring; d,h) experimental and
14 241 calculated LHC intensity, distributed according to the bright central spot; i,l) experimental and
15 242 calculated polarization ellipse parameter $\varepsilon(k_x, k_y)$ indicating a substantially circular polarization, with
16 243 handedness reversal from the central spot to the outer ring; m) calculated phase of the diffracted field
17 244 with RHC polarization, showing two 2π discontinuities (vortex charge $\ell = -2$); n) calculated phase
18 245 of the diffracted field with LHC polarization, showing a uniform phase distribution (vortex charge
19 246 $\ell = 0$).
20 247
21 248

22 249 The distribution of the parameter $\varepsilon(k_x, k_y)$ indicates that the polarization is substantially circular
23 250 across the pattern. However, the bright central spot shows a LHC polarization state, which is reversed
24 251 with respect to the incident radiation (Figure 5i). Furthermore, the outer weak ring maintains a LHC
25 252 polarization, as the illumination (Figure 5l). The conservation of the momentum J leads to $\sigma_i + m =$
26 253 $+1 - 2 = \sigma_o + \ell = -1$, which has the following two solutions associated to the observed beams: σ_o
27 254 $= +1$ (RHC) and $\ell = -2$; $\sigma_o = -1$ (LHC) and $\ell = 0$. The calculated phase distributions are
28 255 consistent with the Total Angular Momentum algebra, since the RHC beam has a vortex wavefront
29 256 with two 2π discontinuities, while the LHC beam has a flat wavefront (Figures 5m,n). A constant
30 257 phase is also consistent with the existence of a central maximum at $k_x = k_y = 0$ for the LHC beam
31 258 (similar situation as in Figure 2m, with a RHC polarization).
32 259

33 260 For a LHC polarization ($\sigma_i = -1$) a phase singularity is produced on the optical axis, and the overall
34 261 intensity pattern (Figures 6a,e) results from the superposition of a RHC polarized vortex of charge
35 262 $\ell = -4$ (Figures 6c,g,m) and a LHC polarized vortex of charge $\ell = -2$ (Figures 6d,h,n).

[FIGURE 6]

Figure 6. BFP Diffraction patterns from a 2-arm spiral outcoupler ($m = -2$). Incident polarization is LHC. a,e) experimental and calculated total intensity; b,f) experimental and calculated x-polarized intensity; c,g) experimental and calculated RHC intensity; d,h) experimental and calculated LHC intensity; i,l) experimental and calculated polarization ellipse parameter $\varepsilon(k_x, k_y)$; m) calculated phase of the diffracted field with RHC polarization showing four 2π discontinuities (vortex charge $\ell = -4$); n) calculated phase of the diffracted field with LHC polarization, showing two 2π discontinuities (vortex charge $\ell = -2$).

Measured and calculated $\varepsilon(k_x, k_y)$ show the handedness reversal occurring when departing from the optical axis toward larger propagation angles, wherein the inner ring preserves the same polarization handedness as the incident radiation (Figures 6i,l). From the conservation of the momentum J , we have: $\sigma_i + m = -1 - 2 = \sigma_o + \ell = -3$, whose solutions are: $\sigma_o = +1$ (RHC) and $\ell = -4$; $\sigma_o = -1$ (LHC) and $\ell = -2$, in accordance to the results shown in Figure 6.

CONCLUSION

To conclude, a new mechanism for the generation of vectorial vortex beams has been presented, based on spin-orbit interactions involving coupling and diffraction of BSWs. Generally speaking, this kind of effects relies on the coherence characteristics of the radiation involved. For this reason, we employed a laser beam as an external free-space radiation for coupling BSWs that are subsequently diffracted, with an imparted azimuthal phase profile. Several combinations of polarization states and OAM are obtained, as summarized in Table 1. Further options for vortex beam generation carrying OAM with other polarization configurations can be possibly produced by means of multilayers supporting TM-polarized, in addition to TE-polarized BSWs.⁴⁶ Moreover, the efficiency of the vortex beam generation can be improved by properly shaping the angular spectrum of the incident radiation, for example as a Bessel beam.⁴⁷

	Grating Topological Charge m	$m = 0$	$m = -1$	$m = -2$
Incident SAM σ_i				
$\sigma_i = +1$		$\sigma_o = -1$ & $\ell = +2$ $\sigma_o = +1$ & $\ell = 0$	$\sigma_o = -1$ & $\ell = +1$ $\sigma_o = +1$ & $\ell = -1$	$\sigma_o = -1$ & $\ell = 0$ $\sigma_o = +1$ & $\ell = -2$
$\sigma_i = -1$		$\sigma_o = -1$ & $\ell = 0$ $\sigma_o = +1$ & $\ell = -2$	$\sigma_o = -1$ & $\ell = -1$ $\sigma_o = +1$ & $\ell = -3$	$\sigma_o = -1$ & $\ell = -2$ $\sigma_o = +1$ & $\ell = -4$

Table 1. Summary of the SAM-OAM combinations obtained by diffraction of BSWs coupled from either RHC or LHC polarized incident light.

The numerical model developed here suggests that the presented approach is likely to work regardless of the coupling mechanism for BSWs. For example, in the perspective of advanced engineered light sources for free-space applications, BSWs can be launched from a single emitter on the multilayer surface by virtue of near-field interactions (so-called BSW-coupled emission).^{48,49} Then, chiral diffractive structures can be used as outcouplers surrounding single point-like sources or even planar BSW cavities (e.g. as described in ref.⁵⁰) hosting light sources within. Provided the coherence requirements for the BSW-coupled radiation leaking out of the cavity are satisfied, the diffraction mechanism for free-space vortex generation remains as reported in the text above. While cavities can be chiral themselves, with a handedness-dependent Local Density of States,⁵¹ it has been recently shown that chiral plasmonic structures can foster sources located on their surface to radiate according to a specific circular polarization handedness.⁵² These strategies provide an unprecedented degree of control on the polarization state of the emitted light. The use of BSWs as a mean for coupling and transferring energy from sources to free-space, mediated by chiral diffractive gratings, can contribute to enhance the performance of purely plasmonic nanostructures, which are often limited by the strong absorption of metals occurring at visible frequencies.

1
2
3
4
5
6
7
8
9
10
11
12
13
14
15
16
17
18
19
20
21
22
23
24
25
26
27
28
29
30
31
32
33
34
35
36
37
38
39
40
41
42
43
44
45
46
47
48
49
50
51
52
53
54
55
56
57
58
59
60

310 METHODS

311 **Experimental setup.** A TEM₀₀ doubled-frequency Nd:YAG laser beam (GEM, Laser Quantum) is
312 collimated (L_1) and transmitted through a first polarization-control box, consisting of a linear
313 polarizer LP₁ and a quarter wave plate QW₁. Circular polarization states with both handedness (RH
314 and LH) are generally produced. A beam blocker is introduced in order to spatially filter the laser
315 beam, such that an illumination above the glass/air critical angle θ_c is provided only. The incoming
316 beam is focused onto a flat area on the top surface of the multilayer through a $NA = 1.49$ objective
317 (Nikon Apo TIRF 1003) that is back-contacted to the glass substrate of the sample. The focused spot
318 has a transverse size much smaller than the diameter of the central flat region of the grating. In this
319 way, the BSW coupling mechanism is resulting from a momentum-matching condition solely ruled
320 by refraction. The sample holder is mounted on a 3-axis piezo stage. When measuring the diffraction
321 patterns from the spiral gratings, the excitation laser is accurately focused onto the geometric center
322 of the diffraction gratings. Diffracted light on the glass side is collected by the same objective and
323 directed toward the collection arm of the setup, after passing through a 50/50 beam splitter. A second
324 polarization-control box consisting of a quarter wave plate QW₂ and a linear polarizer LP₂ filters the
325 outgoing wave onto the desired polarization state (RHC, LHC or LP). Subsequently, the lens L4
326 images the BFP of the objective onto a CMOS camera (Thorlabs HR-CMOS DCC3260M). With no
327 Beam Blocker, an interference pattern appears in the BFP image, due to the superposition of the light
328 reflected by the multilayer inside the light cone ($NA \leq 1$) with the diffracted BSW patterns,
329 eventually carrying OAM. As a result, spiral-like interference fringes can be observed depending on
330 the OAM number ℓ , as shown in Figure S3.³⁵

331 **Sample fabrication.** The 1DPC consists of a dielectric multilayer made of a stack of Ta₂O₅ (high
332 refractive index) and SiO₂ (low refractive index) layers, deposited on a glass coverslip (150 μm
333 thickness) by plasma ion-assisted deposition under high vacuum conditions (APS904 coating system,
334 Leybold Optics). The stack sequence is substrate-[Ta₂O₅-SiO₂]_{x6}-Ta₂O₅-SiO₂-PMMA with 15 layers
335 in total, including PMMA. The Ta₂O₅ layer (refractive index $n_{\text{Ta}_2\text{O}_5}=2.08$) is 95 nm thick, the SiO₂

1
2
3 336 layer (refractive index $n_{\text{SiO}_2}=1.46$) is 137 nm thick. The top SiO_2 layer on top of the stack is 127 nm
4
5 337 thick. On top of the structure a 75 nm thick layer of PMMA is spun for pattern fabrication
6
7
8 338 ($n_{\text{PMMA}}=1.48$). Chiral diffractive structures are fabricated by electron beam lithography.

9
10 339 **Numerical modeling.** Numerical modeling is performed using the Finite-Difference Time-Domain
11
12 340 method in the Lumerical Inc. software. In order to mimic the focused circularly polarized light
13
14
15 341 coupling to BSWs, a pair of orthogonal dipolar emitters are positioned at the geometric center of the
16
17 342 spiral grating. More specifically, the emitters are placed 10 nm above the PMMA layer, with the
18
19 343 dipole momentum laying parallel to the multilayer surface, such that the TE polarization of the BSW
20
21
22 344 can be matched. The two oscillators are phase-shifted by $\pm \pi/2$. In this way, thanks to a near-field
23
24 345 interaction, part of the radiated energy from the dipoles is transferred to BSWs (BSW-coupled
25
26 346 emission). As shown in Figure S1 and Supporting Movie S2, resulting BSWs are radially propagating,
27
28
29 347 with a spiral wavefront due to the time-varying polarization matching conditions of the field given
30
31 348 by the coherent sum of the radiation from the two dipoles.

32
33 349 The diffraction gratings are modeled as circular or spiral grooves in the PMMA layers, with a spatial
34
35 350 period $\Lambda=450$ nm. The total simulation region has dimensions $(15 \times 15 \times 2.6) \mu\text{m}^3$. Boundary
36
37
38 351 conditions are set as perfectly matched layers. The smallest mesh size is 23 nm. The electromagnetic
39
40 352 near-field is collected using a spatial monitor over a plane 20 nm above the PMMA layer. A near-to
41
42
43 353 far-field projection technique is applied to calculate the field at a distance of 1 m from the structure,
44
45 354 on the air side. A cylindrical Perfect Electric Conductor, placed 50 nm above the dipole sources, have
46
47 355 been introduced in order to avoid the direct free-space emission from the sources, which could
48
49 356 produce interference with the BSW-diffracted radiation we want to investigate. This metallic plate
50
51
52 357 mimic the role of the Beam Blocker in the experimental setup. With this arrangement, only the air-
53
54 358 side far-field patterns are calculated. However, as the propagation angles of the diffracted beams (with
55
56 359 respect to the multilayer normal) are very small, the refraction effects are negligible and the far-field
57
58
59 360 patterns are expected to be similar to those on the glass substrate side.

60
361

1
2
3
4
5
6
7
8
9
10
11
12
13
14
15
16
17
18
19
20
21
22
23
24
25
26
27
28
29
30
31
32
33
34
35
36
37
38
39
40
41
42
43
44
45
46
47
48
49
50
51
52
53
54
55
56
57
58
59
60

362 **ACKNOWLEDGEMENTS**

363 This research has been supported by the Région Bourgogne Franche-Comté, the EIPHI Graduate
364 School (ANR-17-EURE-0002), the French Agency of Research (ANR-18-CE42-0016) and by grants
365 R01 GM125976 and R21 GM129561 from the National Institutes of Health. Part of this work has
366 been carried out at Nanofacility INRiM, a laboratory supported by the Compagnia di San Paolo
367 foundation.

369 **SUPPORTING INFORMATION**

- 370 - 3D model of the geometry employed in FDTD simulations, interference patterns for vortex beams
371 with different topological charges, experimental and calculated polarization-filtered intensities and
372 corresponding Stokes parameter distributions of diffracted vortex beams (PDF).
- 373 - Calculated FDTD propagation of the BSW electric field coupled from a pair of $\pi/2$ -phase delayed
374 orthogonal dipoles on a flat multilayer surface (MP4).

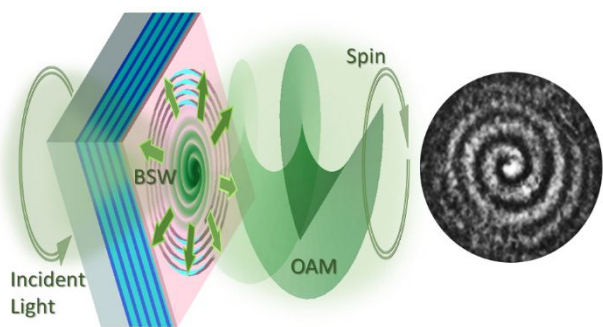
1
2
3 375 **REFERENCES**

- 4
5 376 (1) Yao, A.M.; Padgett, M.J. Orbital angular momentum: origins, behavior and applications. *Adv.*
6 377 *Opt. Photon.* **2011**, 3, 161-204.
- 7
8 378 (2) Shen, Y.; Wang, X.; Xie, Z.; Min, C.; Fu, X.; Liu, Q.; Gong, M.; Yuan, X. Optical vortices 30
9 379 years on: OAM manipulation from topological charge to multiple singularities. *Light: Science*
10 380 *& Applications* **2019**, 8, 90.
- 11
12 381 (3) Yi, X.; Liu, Y.; Ling, X.; Zhou, X.; Ke, Y.; Luo, H.; Wen, S.; Fan, D. Hybrid-order Poincare
13 382 sphere. *Physical Review A* **2015**, 91, 023801.
- 14
15 383 (4) Ng, J.; Lin, Z.; Chan, C.T. Theory of Optical Trapping by an Optical Vortex Beam. *Physical*
16 384 *Review Letters* **2010**, 104, 103601.
- 17
18 385 (5) Cojoc, D.; Garbin, V.; Ferrari, E.; Businaro, L.; Romanato, F.; Di Fabrizio, E. Laser trapping
19 386 and micro-manipulation using optical vortices, *Microelectronic Engineering* **2005**, 78–79, 125–
20 387 131.
- 21
22 388 (6) Ma, Y.; Rui, G.; Gu, B.; Cui, Y. Trapping and manipulation of nanoparticles using multifocal
23 389 optical vortex metalens. *Scientific Reports* **2017**, 7, 14611.
- 24
25 390 (7) Cai, X.; Wang, J.; Strain, M.J.; Johnson-Morris, B.; Zhu, J.; Sorel, M.; O'Brien, J.L.;
26 391 Thompson, M.G.; Yu, S. Integrated compact optical vortex beam emitters. *Science* **2012**, 6,
27 392 338-363.
- 28
29 393 (8) Xie, Z.; Lei, T.; Li, F.; Qiu, H.; Zhang, Z.; Wang, H.; Min, C.; Du, L.; Li, Z.; Yuan, X. Ultra-
30 394 broadband on-chip twisted light emitter for optical communications. *Light: Science &*
31 395 *Applications* **2018**, 7, 18001
- 32
33 396 (9) Wei, S.; Lei, T.; Du, L.; Zhang, C.; Chen, H.; Yang, Y.; Zhu, S.W.; Yuan, X.-C. Sub-100nm
34 397 resolution PSIM by utilizing modified optical vortices with fractional topological charges for
35 398 precise phase shifting. *Optics Express* **2015**, 23, 30143-30148.
- 36
37 399 (10) Chen, L. X.; Lei, J.J.; Romero, J. Quantum digital spiral imaging. *Light: Science & Applications*
38 400 **2014**, 3, e153.
- 39
40 401 (11) Wang, J.; Yang, J.-Y.; Fazal, I.M.; Ahmed, N.; Yan, Y.; Huang, H.; Ren, Y.; Yue, Y.; Dolinar,
41 402 S.; Tur, M.; Willner, A.E. Terabit free-space data transmission employing orbital angular
42 403 momentum multiplexing. *Nature Photonics* **2012**, 6, 488–496.
- 43
44 404 (12) Ruffato, G.; Massari, M.; Romanato, F. Diffractive optics for combined spatial-and mode-
45 405 division demultiplexing of optical vortices: design, fabrication and optical characterization.
46 406 *Scientific reports* **2016**, 6, 24760.
- 47
48 407 (13) Wang, X.; Nie, Z.; Liang, Y.; Wang, J.; Li, T.; Jia, B. Recent advances on optical vortex
49 408 generation. *Nanophotonics* **2018**, 7, 1533-1556.

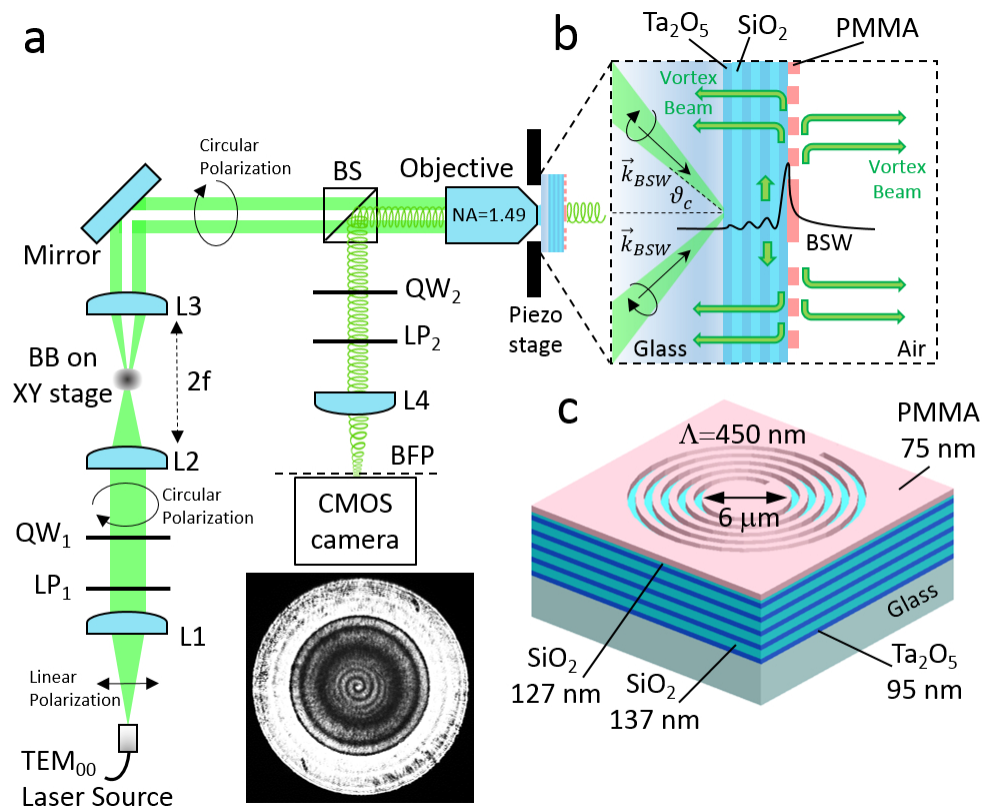
- 1
2
3 409 (14) Marrucci, L.; Manzo, C.; Paparo, D. Optical Spin-to-Orbital Angular Momentum Conversion
4 in Inhomogeneous Anisotropic Media. *Physical Review Letters* **2006**, 96, 163905.
5 410
6 411 (15) Moreno, I.; Davis, J.; Ruiz, I.; Cottrell, D. Decomposition of radially and azimuthally polarized
7 beams using a circular-polarization and vortex-sensing diffraction grating. *Optics Express*
8 **2010**, 18, 7173-7183.
9 412
10 413
11 414 (16) Cardano, F.; Karimi, E.; Slussarenko, S.; Marrucci, L.; de Lisio, C.; Santamato, E. Polarization
12 pattern of vector vortex beams generated by q-plates with different topological charges. *Applied*
13 *Optics* **2012**, 51, C1-C6.
14 415
15 416
16 417 (17) Genevet, P.; Lin, J.; Kats, M.A.; Capasso, F. Holographic detection of the orbital angular
17 momentum of light with plasmonic photodiodes. *Nature Communications* **2012**, 3, 1278.
18 418
19 419 (18) Lin, J.; Genevet, P.; Kats, M.A.; Antoniou, N.; Capasso, F. Nanostructured holograms for
20 broadband manipulation of vector beams. *Nano Letters* **2013**, 13, 4269-4274.
21 420
22 421 (19) Zhan, A.; Colburn, S.; Trivedi, R.; Fryett, T.K.; Dodson, C.M.; Majumdar, A. Low-Contrast
23 Dielectric Metasurface Optics. *ACS Photonics* **2016**, 3, 209-214.
24 422
25 423 (20) Zhou, Y.; Gao, H.; Teng, J.; Luo, X.; Hong, M. Orbital angular momentum generation via a
26 spiral phase microsphere. *Optics Letters* **2018**, 43, 34-37.
27 424
28 425 (21) Yue, F.; Wen, D.; Xin, J.; Gerardot, B.D.; Li, J.; Chen, X. Vector Vortex Beam Generation with
29 a Single Plasmonic Metasurface. *ACS Photonics* **2016**, 3, 1558-1563.
30 426
31 427 (22) Huang, Y.-W.; Rubin, N.A.; Ambrosio, A.; Shi, Z.; Devlin, R.C.; Qiu, C.-W.; Capasso, F.
32 Versatile total angular momentum generation using cascaded J-plates. *Optics Express* **2019**, 27,
33 7469-7484.
34 428
35 429 (23) Bliokh, K.Y.; Rodríguez-Fortuño, F.J.; Nori, F.; Zayats, A.V. Spin-orbit interactions of light.
36 *Nature Photonics* **2015**, 9, 796-808.
37 430
38 431 (24) Bouchard, F.; De Leon, I.; Schulz, S.A.; Upham, J.; Karimi, E.; Boyd, R.W. Optical spin-to-
39 orbital angular momentum conversion in ultra-thin metasurfaces with arbitrary topological
40 charges. *Applied Physics Letters* **2014**, 105, 101905.
41 432
42 433 (25) Maguid, E.; Chriki, R.; Yannai, M.; Kleiner, V.; Hasman, E.; Friesem, A.A.; Davidson, N.
43 Topologically Controlled Intracavity Laser Modes Based on Pancharatnam-Berry Phase. *ACS*
44 *Photonics* **2018**, 551817-1821.
45 437
46 438 (26) Shalaev, M.I.; Sun, J.; Tsukernik, A.; Pandey, A.; Nikolskiy, K.; Litchinitser, N.M. High-
47 Efficiency All-Dielectric Metasurfaces for Ultracompact Beam Manipulation in Transmission
48 Mode. *Nano Letters* **2015**, 15, 6261-6266.
49 439
50 440
51
52
53
54
55
56
57
58
59
60

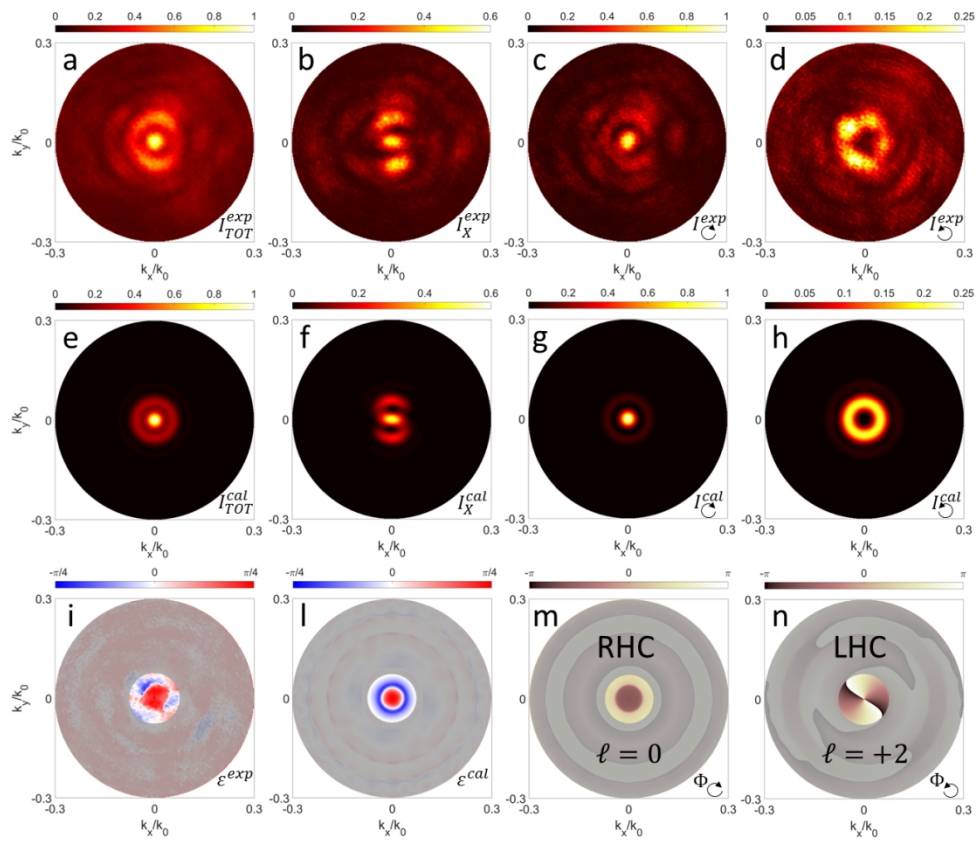
- 1
2
3 441 (27) Ou, K.; Li, G.; Li, T.; Yang, H.; Yu, F.; Chen, J.; Zhao, Z.; Cao, G.; Chen, X.; Lu, W. High
4 efficiency focusing vortex generation and detection with polarization-insensitive dielectric
5 442 metasurfaces. *Nanoscale* **2018**, 10, 19154-19161.
6 443
7
8 444 (28) Yang, Y.; Wang, W.; Moitra, P.; Kravchenko, I.I.; Briggs, D.P.; Valentine, J. Dielectric Meta-
9 Reflectarray for Broadband Linear Polarization Conversion and Optical Vortex Generation.
10 445 *Nano Letters* **2014** 14, 1394-1399.
11 446
12
13 447 (29) Wang, Z.; Wang, Y.; Adamo, G.; Teng, J.; Sun, H. Induced Optical Chirality and Circularly
14 Polarized Emission from Achiral CdSe/ZnS Quantum Dots via Resonantly Coupling with
15 448 Plasmonic Chiral Metasurfaces. *Laser & Photonics Reviews* **2019**, 13, 1800276.
16 449
17
18 450 (30) Rui, G.; Nelson, R.L.; Zhan, Q. Beaming photons with spin and orbital angular momentum via
19 a dipole-coupled plasmonic spiral antenna," *Optics Express* **2012**, 18819-18826.
20 451
21
22 452 (31) Yu, H.; Zhang, H.; Wang, Y.; Han, S.; Yang, H.; Xu, X.; Wang, Z.; Petrov, V.; Wang, J.
23 Optical orbital angular momentum conservation during the transfer process from plasmonic
24 453 vortex lens to light. *Scientific Reports* **2013**, 3, 3191.
25 454
26
27 455 (32) Jiang, Q.; Pham, A.; Berthel, M; Huant, S.; Bellessa, J.; Genet, C.; Drezet, A. Directional and
28 Singular Surface Plasmon Generation in Chiral and Achiral Nanostructures Demonstrated by
29 456 Leakage Radiation Microscopy. *ACS Photonics* **2016**, 3, 1116-1124.
30 457
31
32 458 (33) Gorodetski, Y.; Shitrit, N.; Bretner, I.; Kleiner, V.; Hasman, E. Observation of Optical Spin
33 Symmetry Breaking in Nanoapertures. *Nano Letters* **2009**, 9, 3016-3019.
34 459
35
36 460 (34) Zhang, B.; Hu, C.; Tang, B.; Hao, J.; Zhang, X.; Sun, M.; Ding, J. Chiral plasmonic lens with
37 Archimedes-spiral distributed nanoslits. *Journal of Nanophotonics* **2019**, 13, 026008.
38 461
39
40 462 (35) Gorodetski, Y.; Drezet, A.; Genet, C.; Ebbesen, T.W. Generating Far-Field Orbital Angular
41 463 Momenta from Near-Field Optical Chirality. *Physical Review Letters* **2013**, 110, 203906.
42 464
43
44 464 (36) Robertson, W.M.; May, M.S. Surface electromagnetic wave excitation on one-dimensional
45 465 photonic band-gap arrays. *Applied Physics Letters* **1999**, 74, 1800.
46 466
47
48 466 (37) Liscidini, M.; Galli, M.; Patrini, M.; Loo, R.W.; Goh, M.C.; Ricciardi, C.; Giorgis, F.; Sipe, J.
49 E. Demonstration of diffraction enhancement via Bloch surface waves in a-SiN:H multilayers.
50 468 *Applied Physics Letters* **2009**, 94, 043117.
51 469
52
53 470 (38) Sinibaldi, A.; Fieramosca, A.; Rizzo, R.; Anopchenko, A.; Danz, N.; Munzert, P.; Magistris,
54 C.; Barolo, C.; Michelotti, F. Combining label-free and fluorescence operation of Bloch surface
55 471 wave optical sensors. *Optics Letters* **2014**, 39, 2947-2950.
56 472
57
58 472 (39) Wang, M.; Zhang, H.; Kovalevich, T.; Salut, R.; Kim, M.-S.; Suarez, M.A.; Bernal, M.-P.;
59 473 Herzig, H.-P.; Lu, H.; Grosjean, T. Magnetic spin-orbit interaction of light. *Light Science and*
60 474 *Applications* **2018**, 7, 24.

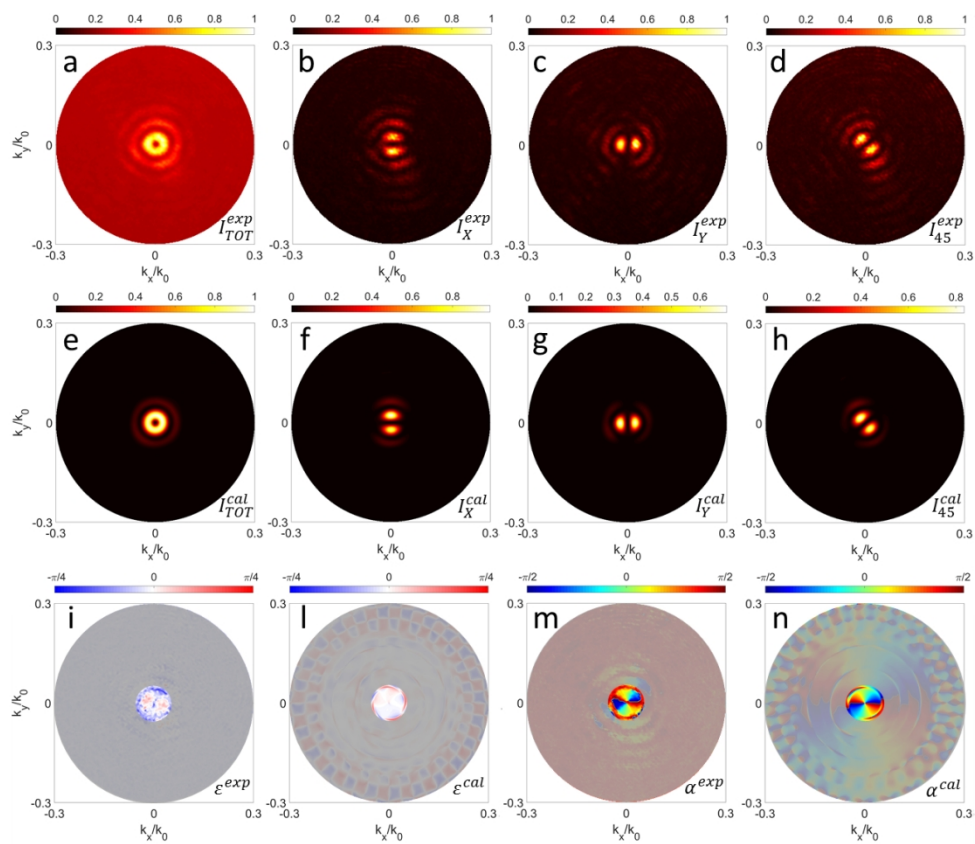
- 1
2
3 475 (40) Angelini, A.; Barakat, E.; Munzert, P.; Boarino, L.; De Leo, N.; Enrico, E.; Giorgis, F.; Herzig,
4 476 H.P.; Pirri, C.F.; Descrovi, E. Focusing and extraction of light mediated by Bloch surface
5 477 waves. *Scientific Reports* **2014**, 4, 5428.
- 8 478 (41) Kim, H.; Park, J.; Cho, S.-W.; Lee, S.-Y.; Kang, M.; Lee, B. Synthesis and Dynamic Switching
9 479 of Surface Plasmon Vortices with Plasmonic Vortex Lens. *Nano Letters* **2010**, 10, 529-536.
- 12 480 (42) Angelini, A.; Enrico, E.; de Leo, N.; Munzert, P.; Boarino, L.; Michelotti, F.; Giorgis, F.;
13 481 Descrovi, E. Fluorescence diffraction assisted by Bloch surface waves on a one-dimensional
14 482 photonic crystal. *New Journal of Physics* **2013**, 15, 073002
- 17 483 (43) Rui, G.; Abeysinghe, D.C.; Nelson, R.L.; Zhan, Q. Demonstration of beam steering via dipole-
18 484 coupled plasmonic spiral antenna. *Scientific Reports* **2013**, 3, 2237.
- 20 485 (44) Angelini, A.; Munzert, P.; Enrico, E.; De Leo, N.; Scaltrito, L.; Boarino, L.; Giorgis, F.;
21 486 Descrovi, E. Surface-Wave-Assisted Beaming of Light Radiation from Localized Sources. *ACS*
22 487 *Photonics* **2014**, 1, 612–617.
- 25 488 (45) Röhrich, R.; Hoekmeijer, C.; Osorio, C.I.; Koenderink, A.F. Quantifying single plasmonic
26 489 nanostructure far-fields with interferometric and polarimetric k-space microscopy. *Light-*
27 489 *Science & Applications* **2018**, 7, 65.
- 30 491 (46) Pellegrini, G.; Finazzi, M.; Celebrano, M.; Duò, L.; Biagioni, P. Chiral surface waves for
31 492 enhanced circular dichroism. *Physical Review B* **2017**, 95, 241402.
- 34 493 (47) Angelini, A. Resonant evanescent complex fields on dielectric multilayers. *Optics Letters* **2015**,
35 494 40, 5746-5749.
- 37 495 (48) Liscidini, M.; Galli, M.; Shi, M.; Dacarro, G.; Patrini, M.; Bajoni, D.; Sipe, J.E. Strong
38 496 modification of light emission from a dye monolayer via Bloch surface waves. *Optics Letters*
39 496 **2009**, 34, 2318-2320.
- 42 498 (49) Badugu, R.; Mao, A.; Blair, S.; Zhang, D.; Descrovi, E.; Angelini, A.; Huo, Y.; Lakowicz, J.R.
43 499 Bloch Surface Wave-Coupled Emission at Ultra-Violet Wavelengths. *Journal of Physical*
44 500 *Chemistry C* **2016**, 120, 28727-28734.
- 47 501 (50) Stella, U.; Boarino, L.; de Leo, N.; Munzert, P.; Descrovi, E. Enhanced directional light
48 502 emission assisted by resonant Bloch Surface Waves in circular cavities. *ACS Photonics* **2019**,
49 503 6, 2073-2082.
- 53 504 (51) Pham, A.; Berthel, M.; Jiang, Q.; Bellessa, J.; Huant, S.; Genet, C.; Drezet, A. Chiral optical
54 505 local density of states in a spiral plasmonic cavity. *Physical Review A* **2016**, 94, 053850.
- 56 506 (52) Pachidis, P.; Cote, B.M.; Ferry, V.E. Tuning the polarization and directionality of
57 507 photoluminescence of achiral quantum dot films with chiral nanorod dimer arrays: implications
58 507 for luminescent applications. *ACS Applied Nano Materials* **2019**, 2, 5681-5687.
- 60 508

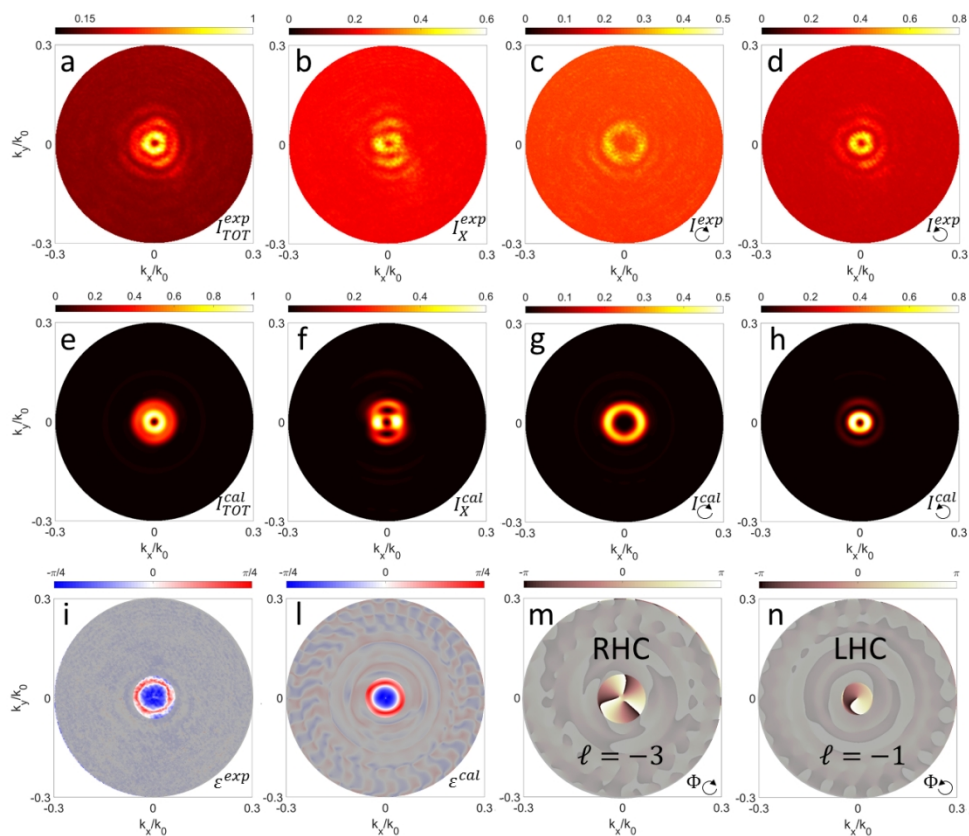
509 **GRAPHICAL TOC ENTRY**

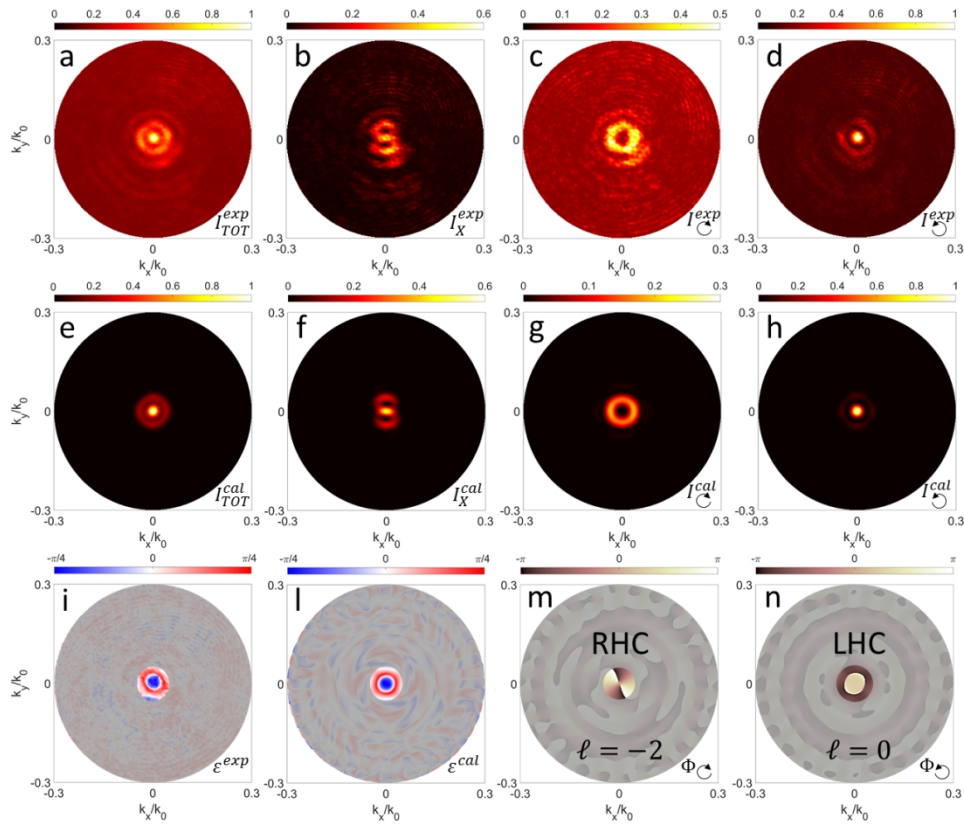
510

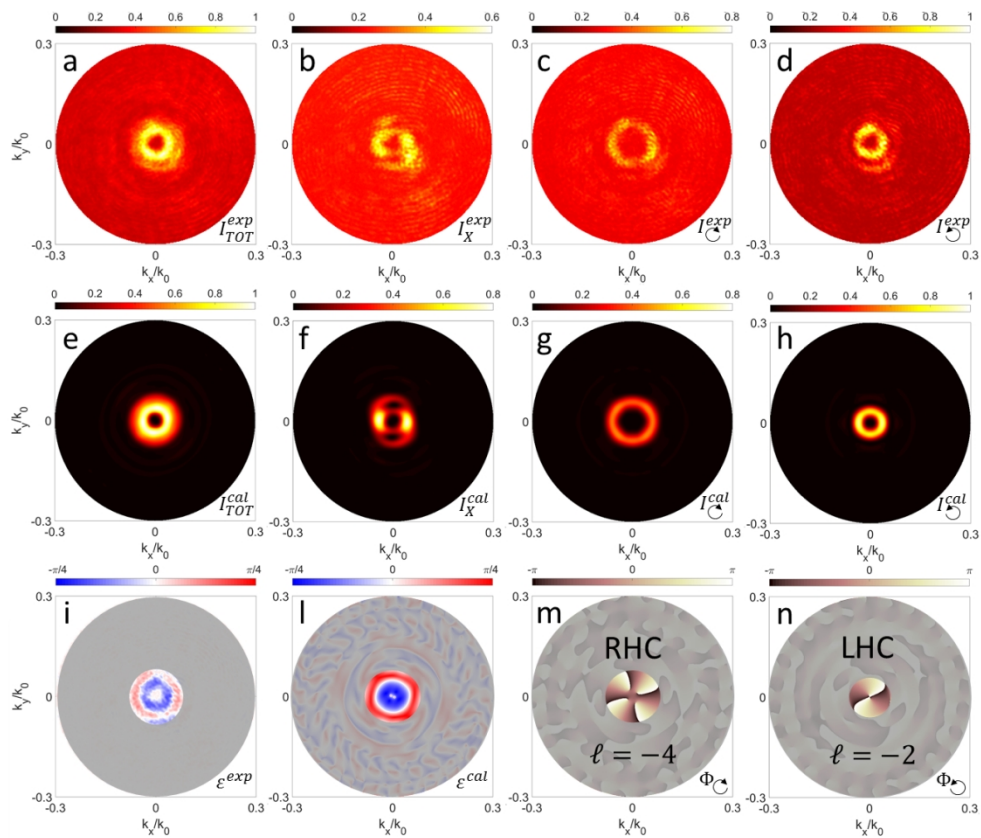




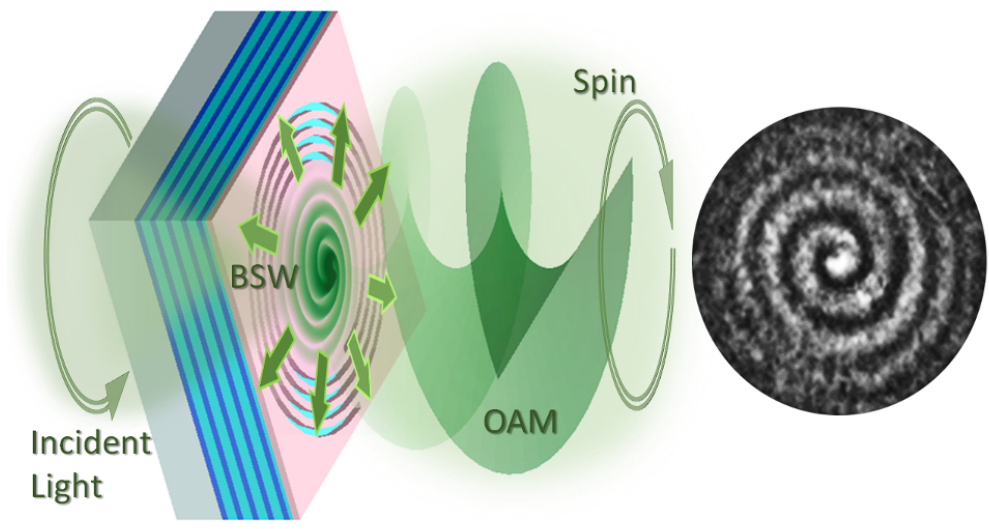








1
2
3
4
5
6
7
8
9
10
11
12
13
14
15
16
17
18
19
20
21
22
23
24
25
26
27
28
29
30
31
32
33
34
35
36
37
38
39
40
41
42
43
44
45
46
47
48
49
50
51
52
53
54
55
56
57
58
59
60



81x44mm (300 x 300 DPI)